The complete Raman spectrum of nanometric SnO_2 particles

A. Diéguez,[a] A. Romano-Rodríguez, A. Vilà, and J. R. Morante
Electronic Materials and Engineering, Department of Electronics, University of Barcelona, C/Martí Franqués, 1, E-08028 Barcelona, Spain

(Received 4 December 2000; accepted for publication 21 May 2001)

The complete Raman spectrum of SnO_2 nanoparticles in presented and analyzed. In addition to the ''classical'' modes observed in the rutile structure, two other regions shown Raman activity for nanoparticles. The Raman bands in the low-frequency region are attributed to acoustic modes associated with the vibration of the individual nanoparticle as a whole. The high-frequency region is activated by surface disorder. A detailed analysis of these regions and the changes in the normal modes of SnO_2 are presented as a function nanoparticle size. © *2001 American Institute of Physics.* [DOI: 10.1063/1.1385573]

I. INTRODUCTION

Tin dioxide has a tetragonal rutile crystalline structure (known in its mineral form as cassiterite) with point group D_{4h}^{14} and space group $P4_2/mnm$. The unit cell consists of two metal atoms and four oxygen atoms. Each metal atom is situated amidst six oxygen atoms which approximately form the corners of a regular octahedron. Oxygen atoms are surrounded by three tin atoms which approximate the corners of an equilateral triangle. The lattice parameters are $a=b=4.737$ Å, and $c=3.186$ Å. The ionic radii for O^{2-} and Sn^{4+} are 1.40 and 0.71 Å, respectively.[1]

The 6 unit cell atoms give a total of 18 branches for the vibrational modes in the first Brillouin zone. The mechanical representation of the normal vibration modes at the center of the Brillouin zone is given by[2,3]

$$\Gamma=\Gamma_1^+(A_{1g})+\Gamma_2^+(A_{2g})+\Gamma_3^+(B_{1g})+\Gamma_4^+(B_{2g}) +\Gamma_5^-(E_g)+2\Gamma_1^-(A_{2u})+2\Gamma_4^-(B_{1u})+4\Gamma_5^+(E_u), \quad (1)$$

using the Koster notation with the commonly used symmetry designations listed in parenthesis. The latter will be used throughout this article.

Of these 18 modes, 2 are active in infrared (the single A_{2u} and the triply degenerate E_u), 4 are Raman active (three nondegenerated modes, A_{1g}, B_{1g}, B_{2g}, and a doubly degenerate E_g), and two are silent (A_{2g}, and B_{1u}). One A_{2u} and two E_u modes are acoustic. In the Raman active modes oxygen atoms vibrate while Sn atoms are at rest (see Fig. 1 in Ref. 4). The nondegenerate mode, A_{1g} , B_{1g}, and B_{2g}, vibrate in the plane perpendicular to the c axis while the doubly degenerated E_g mode vibrates in the direction of the c axis. The B_{1g} mode consists of rotation of the oxygen atoms around the c axis, with all six oxygen atoms of the octahedra participating in the vibration. In the A_{2g} infrared active mode, Sn and oxygen atoms vibrate in the c axis direction, and in the E_u mode both Sn and O atoms vibrate in the plane perpendicular to the c axis. The silent modes correspond to vibrations of the Sn and O atoms in the direction of the c axis (B_{1u}) or in the plane perpendicular to this direction (A_{2g}).

According to the literature, the corresponding calculated or observed frequencies of the optical modes are presented in Table I. When the size of the SnO_2 crystal is reduced, the infrared spectrum is modified because the interaction between electromagnetic radiation and the particles depends on the crystal's size, shape, and state of aggregation.[8–10] Experiments using Raman spectroscopy have also reported spectrum modification, at least partially. Low frequency bands have been observed previously in SnO_2,[11] and several authors have reported the existence of bands not observed in single-crystal or polycrystalline SnO_2 which have been found to be closely related to grain size.[12–15] However, some of these reports do not adequately explain the origin of the abnormal spectrum.

The aim of this article is to present a complete Raman spectrum of SnO_2 nanoparticles. The analysis comprises (i) modification of the normal vibration modes active in Raman when the spectra are obtained from nanocrystals of SnO_2 (''classical modes''), (ii) the disorder activated surface modes in the region around 475–775 cm^{-1}, and (iii) the appearance of the acoustic modes in the low-frequency region of the spectra.

II. EXPERIMENT

Nanocrystalline SnO_2 powder was prepared by first adding ammonia to an aqueous tin chloride solution. The precipitated gel was then repeatedly washed in bidistilled water to remove chlorine contamination. A white powder or hydrated tin oxide is thus obtained which is then calcinated for 8 h at temperatures ranging from 250 to 1000 °C.

Raman scattering measurements were obtained by backscattering geometry with a Jobin–Yvon T64000 spectrometer coupled to an Olympus metallographic microscope. Excitation was provided by an argon-ion laser operated at a wavelength of 488.0 or 457.5 nm and a low incident power to avoid thermal effects. Raman shifts were corrected by using silicon reference spectra after each measurement of SnO_2.

Transmission electron microscopy (TEM), x-ray diffraction (XRD), and Fourier-transform infrared (FTIR) spectroscopy were also used. TEM measurements were used to de-

[a]Electronic mail: dieguez@el.ub.es

TABLE I. Frequencies of the different optical modes of SnO_2. Three references have been considered enough to report all of them. In the three references large crystals were examined. A superscript * indicates that the value has been calculated. (TO is transverse optical and LO is longitudinal optical.)

					A_{2u}			E_u		
A_{1g}	B_{2g}	B_{1g}	A_{2g}	E_g	TO	LO	B_{1u}	TO	LO	Reference
638	782	100*	398*	476	477	705	140*	244	276	5
							505*	293	366	
								618	710	
					465	704		243	273	6
								284	368	
								605	757	
634	776	123		475						7

termine the grain size distribution of the powders, XRD to analyze crystalline quality, and FTIR to measure the water content of the samples.

TEM measurements were taken using a Philips CM30 SuperTwin electron microscope operating at 300 keV. For TEM examination the powders were ultrasonically dispersed in ethanol and deposited onto amorphous carbon membranes.

X-ray diffraction was measured with an INEL powder diffractometer using Cu $K\alpha$ radiation, in Debye–Scherrer geometry, with a position sensitive detector of 120° 2θ and a quartz primary monochromator to eliminate the $K\alpha_1$ radiation, and with a Siemens D-500 diffractometer, in Bragg–Brentano $\theta/2\theta$ geometry, also using Cu $K\alpha$ radiation.

FTIR transmission measurements were taken with a Bomem MB-120 spectrometer. The spectra were measured at room temperature using normal incidence and had a spectral resolution of 1.9 cm^{-1}. Absorption spectra from the samples were extracted using the reference spectra of air. The FTIR spectra from the powders were obtained by the usual method of pressing them into KBr pellets.

III. RESULTS AND DISCUSSION

Figure 1 shows the complete Raman spectrum of the different powders analyzed. For purposes of clarity the spectra have been divided into two regions. Powders composed of nanoparticles smaller than ~7 nm show bands in the low-frequency region [Fig. 1(a)] while for larger particles ($T_{\text{calcination}} = 1000\,°C$), the Raman spectra show contributions only in the high-frequency region, the ''classical'' modes of SnO_2 being seen here. However, with nanoparticles smaller than ~16 nm, other contributions are also visible in the high-frequency zone [Fig. 1(b)]. Figure 2 shows a typical configuration for all contributions in this region for powder calcinated at 400 °C. The nanoparticle size and the different band frequencies seen in the spectra are given in Table II.

It can be seen that the Raman spectrum depends to a large extent on the temperature at which the initially obtained oxide was calcinated, i.e., on the size of the nanoparticles. The general features of the spectra are the following.

(1) The mode A_{1g} shifts to lower wave numbers as the nanoparticle size decreases. At the same time modes B_{2g} and E_g approach A_{1g}, i.e., they shift toward lower and higher wave numbers, respectively. However, the variation of the mode E_g is very small. The shift is accompanied by broadening of the band. Mode B_{1g} appears quite often with smaller nanoparticles but is difficult to locate due to its very low intensity with respect to the other modes [$0.001I(A_{1g})$] (Ref. 7) and the existence of the low-frequency bands.

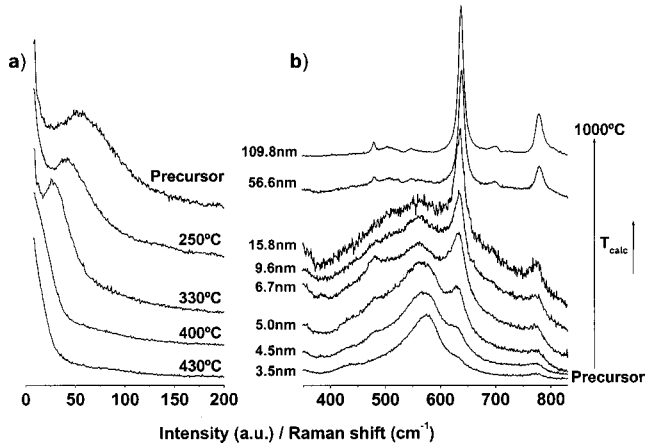

FIG. 1. Raman spectra of the powders calcinated up to 1000 °C for 8 h. The spectra have been divided into the low-frequency region (a) and the high-frequency region (b). The spectra in the high-frequency region correspond, from bottom to top, to the uncalcinated powder and the powders calcinated at 250, 330, 400, 430, 450, 800, and 1000 °C for 8 h. Additional features were not observed outside these regions.

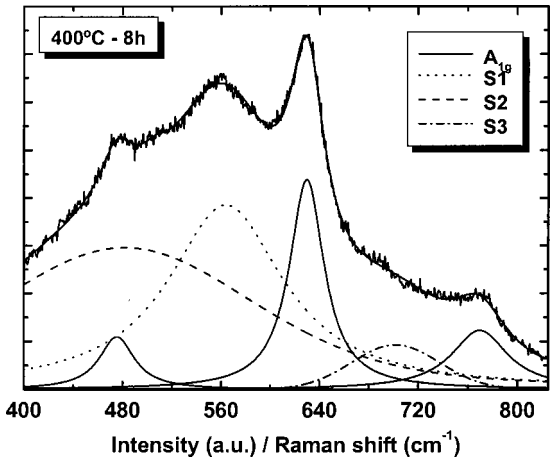

FIG. 2. Fitting of the bands appearing in the high-frequency region of the Raman spectrum of a SnO_2 powder of very small grain size. The bands peaking at ~634, 568, 486, and 706 cm^{-1} correspond to mode A_{1g} and bands $S1$, $S2$, and $S3$, respectively. Modes B_{2g}, peaking at ~776 cm^{-1}, and E_g, peaking at 480 cm^{-1}, are also included in the fitting.

TABLE II. Raman shift of the most important bands observed in the SnO_2 nanoparticle spectrum. Modes A_{1g}, B_{2g}, and E_g correspond to the classical vibration modes while bands $S1$, $S2$, and $S3$ appear as a consequence of disorder activation. LFRB refers to the bands appearing in the low-frequency region of the spectrum. A_S/A_{A1g} corresponds to the sum of the areas of bands $S1$ and $S2$ with respect to the area of the band corresponding to the A_{1g} mode. The values given for nanoparticle size result from detailed statistics (in some cases more than 500 measurements) and the use of imaging processing software.

T (°C)	L (nm)	A_{1g}	B_{2g}	E_g	$S1$	$S2$	$S3(A_{2u})$	A_S/A_{A1g}	LFRB
1000	109.8	637.9	779.2	479.2	⋯	⋯	⋯	⋯	
800	56.6	637.9	778.9	479.5	⋯	⋯	⋯	⋯	
450	15.8	635.2	774.2	479.7	568.9	493.2	696.3	1.32	
430	9.6	634.3	774.1	479.6	568.0	501.2	706.9	4.07	16.4
400	6.7	633.9	776.2	479.6	568.1	485.9	705.8	5.82	21.7
330	5.0	633.1	772.9	⋯	572.0	503.7	691.7	10.02	33.4
250	4.5	631.6	767.7	⋯	573.3	518.0	⋯	14.79	44.5
Room temperature	3.5	631.5	⋯	⋯	575.8	541.7	⋯	47.17	58.3

(2) The presence of several bands in the region between 475 and 775 cm^{-1} ($S1$, $S2$, and $S3$ in Fig. 2). The intensity and position of these bands also depend on the nanoparticle size. The tendency of bands $S1$ and $S2$ is always to decrease in intensity and position as the nanoparticle size increases. No evidence of a shift has been found in the case of band $S3$.

(3) The appearance of low-frequency bands whose position and intensity depend on the size of the nanoparticles. These bands shift toward higher wave numbers, are less intense, and broaden as the average nanoparticle size decreases. For particles larger than ~7 nm these bands are not observed by simple visual inspection.

Along with these features of the Raman spectra it is worth noting that the XRD spectra and electron diffraction patterns of the different SnO_2 powders suggest a cassiterite crystalline structure even in the as-obtained hydrated oxide obtained here (Fig. 3). The main feature of these spectra is narrowing of the XRD peaks as the calcination temperature is increased, an effect due to an increase in grain size and higher crystalline quality. For low calcination temperatures, high resolution TEM (HRTEM) shows that the nanoparticles are characterized by a quasispherical shape, a strong distortion of the crystalline structure, and a high degree of agglomeration.[11] Likewise, the FTIR spectra of these nanoparticles show the water content as well as hydroxyl absorption bands. Both OH groups and lattice distortion progressively disappear as the calcination temperature is increased, with it being completely absent around 400–450 °C. The nanoparticles calcinated at temperatures higher that 450 °C are of good crystalline quality, deagglomerated and faceted.[10]

In Sec. III A, the different characteristics of the Raman spectra are explained in detail as a function of grain size and disorder.

A. Classical modes of SnO_2

It is well known that in an infinite perfect crystal only the phonons near the center of the Brillouin zone (BZ) ($\mathbf{q}_0 \approx 0$) contribute to the scattering of incident radiation due to the momentum conservation rule between phonons and incident light. As the size of the crystal is reduced, the vibration is limited to the size of the crystal, which gives rise to breakdown of the phonon momentum selection rule $\mathbf{q}_0 \approx 0$, allowing phonons with $\mathbf{q} \neq 0$ to contribute to the Raman spectrum.[16,17] According to the phonon dispersion curves,[7] modes A_{1g} and B_{2g} shift toward lower wave numbers as the nanoparticle size decreases, whereas mode E_g shifts toward higher wave numbers, which is precisely the nanoparticle behavior observed in this study. Table II also shows that it is the B_{2g} mode which varies most quickly. Mode A_{1g} shifts slowly and mode E_g is practically immobile until a strong phonon confinement is considered.

In the spatial correlation model (also known as the phonon confinement model) the localization of the phonons is described by a weighting function $W(\mathbf{r},L)$ for the phonon amplitude, where L is the size of the nanocrystals, and hence the vibrational wave function in a nanocrystal can be approximated by

$$\Psi(\mathbf{q_0},\mathbf{r}) = W(\mathbf{r},L)\Phi(\mathbf{q_0},\mathbf{r}). \tag{2}$$

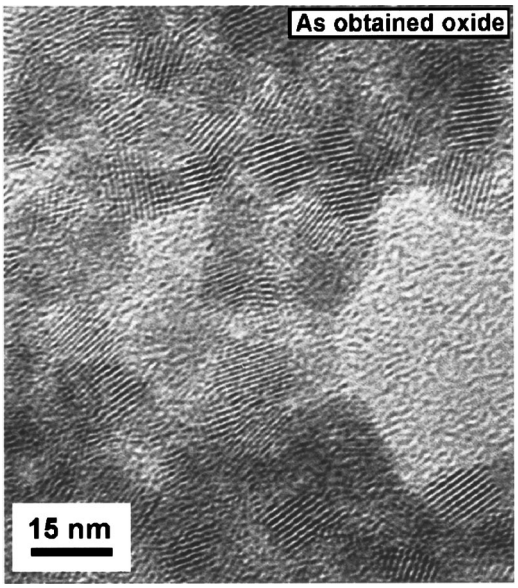

FIG. 3. High-resolution transmission electron microscopy image of the as-obtained hydrated oxide. The nanoparticles are clearly crystalline with a quasispherical shape.

The first-order Raman spectrum of a nanocrystal, $I(\omega)$, is thus given by

$$I(\omega)=\int_{BZ}\frac{|C(\mathbf{q})|^2}{[\omega-\omega(\mathbf{q})]^2+(\Gamma_0/2)^2}d\mathbf{q}, \tag{3}$$

where $\omega(\mathbf{q})$ is the phonon dispersion curve of the infinite crystal, Γ_0 is the natural linewidth, and $C(\mathbf{q})$ are the Fourier coefficients of the vibrational weighting function expanded in a Fourier integral, which will determine the line shape of the Raman bands.

In most cases a Gaussian weighting function is used to describe the Raman spectra of nanoparticles.[18–22] In this case,[22]

$$|C(\mathbf{q})|^2=\frac{L^6}{16(2\pi)^2\alpha^3}e^{-q^2L^2/2\alpha}, \tag{4}$$

with $\alpha=8\pi^2$.

Given that below 400–450 °C the nanoparticles studied here had a quasispherical shape, it seems wise to use this weighting function.

The integration over the entire Brillouin zone can be approximated by an unidimensional integral over a spherical Brillouin zone:

$$I(\omega)\approx\int_0^1\frac{e^{(qL/4\pi)^2}4\pi q^2}{[\omega-\omega(q)]^2+(\Gamma_0/2)^2}dq, \tag{5}$$

where the $4\pi q^2$ term arises from the change into spherical coordinates and integrate over the radius. Hence, the wave vector q and the correlation length L are expressed in units of $2\pi/\langle a\rangle$ and $\langle a\rangle$, respectively, with $\langle a\rangle=(2a+c)/3=0.422$ nm being an average lattice constant for SnO_2. Since no data have been reported for Γ_0, it has been estimated to be about 11.5 cm^{-1} by fitting of the A_{1g} band in the Raman spectrum of the powder calcinated at 1000 °C, which is the nearest to a single SnO_2 crystal. For the fitting a convolution of bands due to the size distribution was not taken into account because, due to the large grain size, this should not influence the spectrum.

For the phonon dispersion curve of the A_{1g} mode we have used a 5° polynomial fitting of the curve in Ref. 7:

$$\omega(q)=A+B_1(q\pi)+B_2(q\pi)^2+B_3(q\pi)^3+B_4(q\pi)^4+B_5(q\pi)^5, \tag{6}$$

with $A=638.22$ cm^{-1}, $B_1=-2.81$ cm^{-1}, $B_2=6.52$ cm^{-2}, $B_3=-7.25$ cm^{-3}, $B_4=0.27$ cm^{-4}, and $B_5=0.21$ cm^{-5}.

The Raman spectra calculated using the spatial correlation model, for nanoparticles between 10 and 110 nm, is shown in Fig. 4. For particles smaller than ~10 nm the calculation produces an exaggerated asymmetrical curve due to interference from the limits of the Brillouin zone.

To easily compare theoretical predictions and experimental data we plotted both the experimental and theoretical Raman shifts and the full width at half maximum (FWHM) as a function of nanoparticle size in Figs. 5(a) and 5(b), respectively. For particles larger than 10–15 nm there is good agreement between the model and experiments. However, for smaller sizes, the experimental points differ from the calculated ones because, as the nanoparticle size decreases, there is an increasing contribution from particles across the size distribution. In the case of large particles, which present a higher volume for Raman scattering, there is no effect due to the size distribution. Other factors which may contribute to the disagreement are the presence of defects, which would reduce the correlation length, L, and disordered regions, contributing partially to the classical modes.

The results indicate that the spatial correlation model is applicable to SnO_2 and can be used to estimate nanoparticle size, as is shown in Fig. 4. However, it should be noted that Fig. 5 gives larger sizes than those extracted by TEM for particles smaller than ~10 nm.

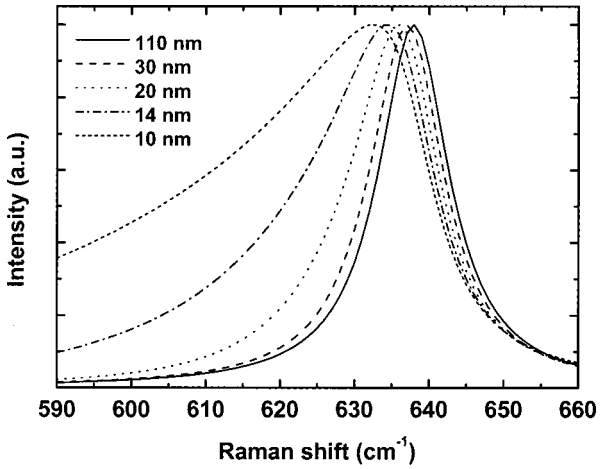

FIG. 4. Calculated Raman spectra for the A_{1g} mode according to the spatial correlation model. The curves correspond to particles with diameters of 110, 30, 20, 14, and 10 nm.

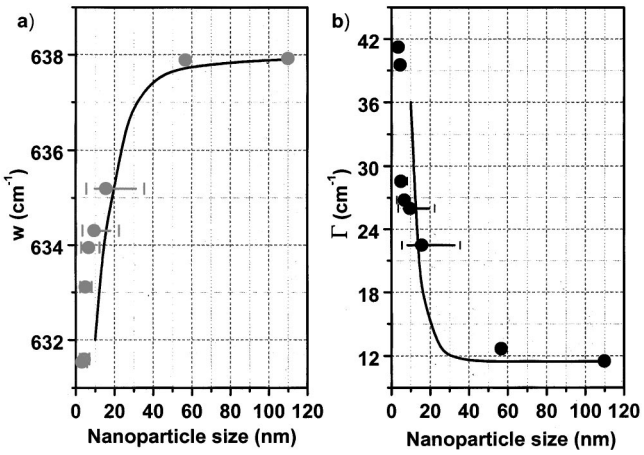

FIG. 5. Calculated (lines) and experimental (points) values of the Raman shift (a) and FWHM (b) as a function of nanoparticle size. Horizontal error bars, shown for powders calcinated at 450 °C or lower, indicate the dispersion of sizes extracted from the histograms. The positions of the points correspond to the average grain size.

B. Modes activated by disorder in SnO_{2-}

As was pointed out earlier, bands other than the classical ones were visible in the high-frequency region and as Table II shows the most important of these appear at 576–568 cm^{-1} ($S1$), 542–486 cm^{-1} ($S2$), and 691–707 cm^{-1} ($S3$). Although it is not clear how many bands have to be used to fit in this region, we have based on the evolution observed in Fig. 1(b) as a function of calcination temperature to find the minimum number of lines needed to perform the analysis. The powder calcinated at 1000 °C (that with particles which are more like single crystal) was fitted with the lines corresponding to the classical modes of the SnO_2 cassiterite. For lower calcination temperatures, up to three additional lines have to be included in the fitting, i.e., bands $S1$, $S2$, and $S3$. $S1$ and $S2$ are always the most intense bands. The shift of the $S3$ band is attributed more to the difficulty in performing the fitting in that region than to a real shift. In theory, this band can be attributed to disorder activation of the A_{2u} IR active and Raman forbidden mode.[15] The evolution of bands $S1$ and $S2$ with decreasing nanoparticle size (calcination temperature) indicates that they arise either as a consequence of reducing particle dimensions or due to the conversion from amorphous to crystalline material. However, since the nanoparticles are crystalline for the complete range of sizes analyzed in this work, the appearance of these bands cannot be due to amorphous material. Other factors such as phonon–plasmon coupling can also be rejected because it is well known that when SnO_2 nanoparticles have very small sizes, the grain is formed to a large extent by a depletion region when exposed to an atmosphere containing oxygen. Therefore, the contribution of bands $S1$ and $S2$ would not increase with decreasing nanoparticle size if their origin was phonon–plasmon coupling.

In a disordered crystal, imperfections modify its symmetry, preventing atoms from vibrating in phase and preventing their displacements to be correlated. Changes in the crystal's local symmetry produce changes in some of the components of the polarizability tensor, even for usually forbidden vibration modes, i.e., due to the loss in long-range order all phonons are optically possible and the Raman spectrum should resemble the phonon density of states. In an intermediate case, a shift of the classical modes accompanied by broadening and the appearance of some of SnO_2's forbidden modes should be observed. This is indeed what occurs with modes A_{1g}, B_{2g}, E_g, and A_{2u}. However, bands $S1$ and $S2$ do not fit any of the Raman forbidden modes of SnO_2 and the appearance of a new mode as a consequence of coupling between modes would not explain the high contribution of these bands observed in the spectrum of the smaller nanoparticles. Furthermore, it is well known that nanometer-sized crystalline materials have a crystalline component forming the crystallite nucleus and an interfacial component consisting of all the atoms situated at the grain boundaries between particles, or at their surfaces. The latter usually has several atomic layers in which atoms are slightly displaced from the exact position that would be suggested by the crystalline structure of the material. Thus, it is possible that bands $S1$ and $S2$ arise from this surface region which, as an approximation, can be considered to be of constant thickness for all samples. To check this hypothesis, Fig. 6 represents the ratio of the summed area of bands $S1$ and $S2$ to the area of the A_{1g} mode. By assuming that each nanocrystal of radius r is composed of a crystalline core of radius $(r-d)$, surrounded by a shell which is a disordered layer of thickness d, the ratio of the volumes corresponding to the scattering by each component is directly related to the ratio of the areas of the Raman bands:

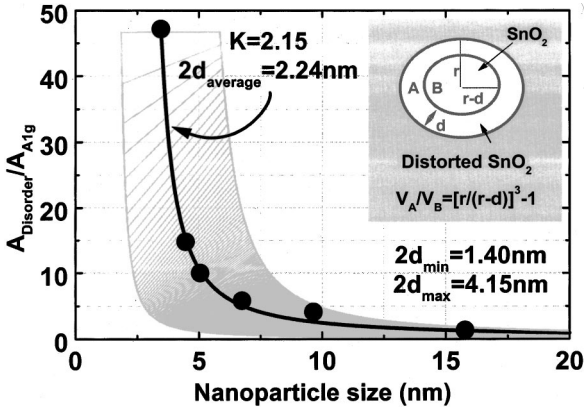

FIG. 6. Ratio of the summed area of bands $S1$ and $S2$ with respect to the area of the band for the A_{1g} mode as a function of nanoparticle size. The dashed area corresponds to the minimum and maximum relevant grain sizes in the TEM histograms. According to the fitting indicated, the thickness of the disordered surface region is ~1.1 nm. The inset shows a schematic of a nanoparticle with radius r, formed by a perfectly crystalline core of radius $r-d$ and a disordered shell of size d.

$$\frac{A_{S1+S2}}{A_{A1g}} \propto \frac{V_{\text{shell}}}{V_{\text{core}}} = K\left[\left(\frac{r}{(r-d)}\right)^3 - 1\right]. \tag{7}$$

As Fig. 6 shows, when the nanoparticle size is reduced, the volume occupied by the interface and surface material increases with respect to the volume occupied by core material. In this way, one can calculate an average thickness for the shell, $d \approx 1.1$ nm, i.e., approximately two to three unit cells of SnO_2, which is in agreement with the usual thickness found for surface layers.[23,24] It has been shown that, in the extreme case of single SnO_2 crystals, surface reconstruction in the (110) surface involves up to three monolayers of atoms and the presence of oxygen vacancies.[25] This gives rise to a nonstoichiometric SnO_x at the surface and this could be responsible for producing bands $S1$ and $S2$. That these bands are observed in SnO_2 and not in other nanocrystalline semiconductors may be due to the high reactivity of the SnO_2 surface with environmental gases, for instance, like when the surface of the nanoparticles is exposed to H_2S, surface phonon bands are considerably reduced.[26] The same experiments[26] suggest that there is no direct relationship between Sn–OH bonds, where the OH comes from water, and hydroxyl isolated groups present at the surface of the nanoparticles, since the Raman bands $S1$ and $S2$, are recovered after purging of the H_2S gas. The high Raman activity of these bands for very small crystals, resulting from disordered SnO_x and, probably, from the interaction of surface material with adsorbed oxygen, can be explained by the findings of Hama and Matsubara[27] and of Hayashi and Yamamoto,[28]

which suggest that the Raman enhancement of the shell contribution is caused by the larger vibrational amplitudes and much higher electric field in the shell than in the core.

The calculated value of d corresponds to an average of the surface region thickness for all particles forming the size distribution, assuming that this thickness is similar for all samples. Although not exact, this would seem to give a better approximation than considering the existence of only one monolayer of atoms in the surface of the nanoparticles,[12,15] especially for the smaller ones.

When the size distribution and the decrease of nanoparticle diameter by $2d$ are taken into account, better agreement is obtained for some points in Fig. 5. However, other mechanisms have to be considered for particles smaller than 8 nm. The existence of surface stresses as a consequence of the bonding of the shell atoms to the core atoms and the presence of adsorbed species at the surface of the nanoparticles could be taken into account for a more exact approximation to this problem.

C. Low frequency modes of SnO_2 nanoparticles

The final features of the Raman spectrum of nanometric SnO_2 are the low-frequency bands observed for particles smaller than 7 nm [Fig. 1(a)]. After correcting for the Bose–Einstein occupation factor and applying the background and Rayleigh line correction, the resulting spectra give bands at ~58, 44, 33, 22, and 16 cm^{-1} for particles of 3.5, 4.5, 5.0, 6.7, and 9.6 nm, respectively, as deduced from TEM micrographs. These bands shift toward higher frequencies and become less intense and broader as the average nanoparticle size decreases. Except for the last powder (9.6 nm), another much less intense band can be found as a shoulder on the previous band at frequencies around 96, 62, 49, and 38 cm^{-1}. The difficulty of experimentally analyzing these bands forces us to focus discussion on the principal ones.

Low-frequency bands have been reported for Ag particles embedded in SiO_2 thin films,[29] CdSe nanocrocrystals in glasses,[30] CdS microcrystals,[31,32] $MgCr_2O_4$–$MgAl_2O_4$ crystals in glass,[33] and nanosized TiO_2.[34] Despite the number of publications related to SnO_2 and Raman spectroscopy, however, they have not generally been reported for SnO_2.[12–15] An exception to this is our previous paper[11] in which we demonstrated them to be an effective way of evaluating not only the average nanoparticle size, but also the whole size distribution.

Phonon dispersion curves for the acoustic branches of SnO_2 predict that Raman bands shift toward higher wave numbers as the nanoparticle size decreases. However, the problem in the low-frequency region is usually considered from a classical point of view by considering the particle's acoustic vibration as a whole. Analysis of these vibrations typically assumes a perfectly spherical elastic body which is homogeneous and isotropic. Thus, acoustic vibrations are characterized by the longitudinal and transverse sound velocities, v_l and v_t, respectively. A theoretical explanation for the origin of such low-frequency vibrations was first introduced by Lamb,[35] extended by Tamura *et al.*,[36] and recently revised by Saviot *et al.*[32] Lamb's theory begins with the equation of motion of a three-dimensional elastic body:

$$\rho \frac{\partial^2 \mathbf{D}}{\partial t^2} = (\lambda + \mu)\nabla(\nabla \cdot \mathbf{D}) + \mu \nabla^2 \mathbf{D}, \tag{8}$$

where $\mathbf{D}$ is the displacement vector, the two parameters λ and μ are Lamé constants, and ρ is the mass density. The solution of this equation (the results can be found in Ref. 11) leads to two types of vibrational mode, spheroidal and torsional. The energy associated with these modes is only a few cm^{-1} and its effects can be measured in the low-frequency region of the Raman spectra. Depending upon the nature of the nanoparticles and the surrounding environment two different boundary conditions have to be considered to solve Eq. (8): "stress free," meaning that no external forces are applied on the particle surface; and "rigid," meaning that no displacement occurs at the particle surface. Whatever the boundary conditions are, the frequency of the vibration is given by

$$\omega = S_{l,n} \frac{v}{Lc}, \tag{9}$$

where v is one of the two sound velocities, depending on the type of vibration (v_l for spheroidal or longitudinal and v_t for torsional or transversal). $S_{l,n}$ is a coefficient depending on the sound velocities, the choice of the boundary condition, and the angular momentum l and harmonic n of the vibration mode, i.e., the order of the roots of Eqs. (2)–(5) in Ref. 11.

TABLE III. Values of S_l and S_t for the rigid and stress-free boundary conditions of the spheroidal modes for $n=1,2$, and 3.

	Rigid		Stress free	
$l=0$	$S_l=1.430$	$n=1$	$S_l=0.887$	$n=1$
	$S_l=2.459$	$n=2$	$S_l=1.952$	$n=2$
	$S_l=3.471$	$n=3$	$S_l=2.969$	$n=3$
$l=2$	$S_t=1.987$	$n=1$	$S_t=0.844$	$n=1$
	$S_t=2.586$	$n=2$	$S_t=1.638$	$n=2$
	$S_t=3.432$	$n=3$	$S_t=2.760$	$n=3$

In the case of SnO_2, solving the previous equations using the average sound velocities of bulk SnO_2,[5] $v_l=6.53\times10^5$ cm s^{-1} and $v_t=3.12\times10^{15}$ cm s^{-1} enable the frequencies of the Raman lines to be estimated using Eq. (9). The values of the coefficients $S_{l,n}$ for the rigid and stress-free boundary conditions needed for the calculation are given in Table III. Theoretical predictions, together with the experimental data, are shown in Fig. 7. Lines represent the theoretical dependence for the rigid and stress-free boundary conditions of the surface modes with $l=0$ and 2. The curves with $l=0$ for the stress-free boundary condition and $l=2$ for the rigid boundary condition approximate well to experimental results, i.e., $l=0$ for the stress-free boundary condition and $l=2$ for the rigid boundary condition.

Figure 7 also shows that low-frequency Raman spectra can be used to analyze the nanoparticle size in SnO_2, regardless of whether it is the stress-free boundary condition and $l=0$ or the rigid boundary and $l=2$ which is applied. It is important to note that by using an averaged theoretical curve

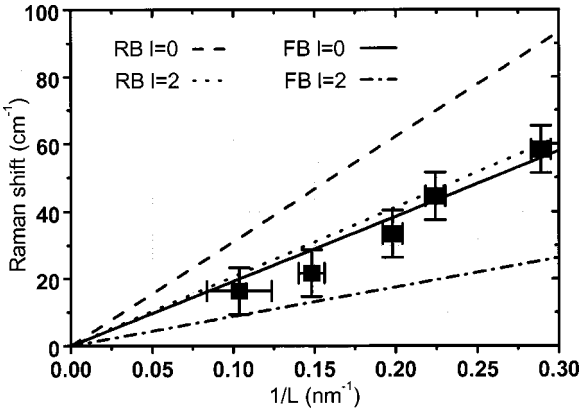

FIG. 7. Experimental and calculated Raman shifts for the different boundary conditions as a function of the inverse of nanoparticle size.

(average of the curve corresponding to the stress-free boundary condition and $l=0$ and that corresponding to the rigid boundary and $l=2$), the grain size distribution can be extracted in a nondestructive way by deconvolution of the theoretical curve with the low-frequency Raman spectra (Fig. 8). There is quite good agreement between the real size of the nanocrystals (extracted by TEM) and the Raman size in the sense that the nanoparticle size distribution obtained by Raman spectroscopy is an envelope of that obtained by TEM, especially for the smaller nanoparticles. The nanoparticles sizes obtained by LFR are therefore 3.5, 4.4, 5.6, 8.8, and 11.4 nm for the as-obtained SnO_2 and the powders calcinated at 250, 330, 400, and 430 °C, respectively. For the larger nanoparticles, the peak position shifts toward lower frequencies, approaching the laser line, and the spectrum is more influenced by the Rayleigh contribution, thus raising doubts about the reliability of the results.

IV. CONCLUSIONS

By analyzing nanoparticles ranging from 3 to 100 nm in size we have been able to describe the whole Raman spectrum of nanometric SnO_2. Disorder and nanoparticle size strongly influence the vibrational properties of this material. When the nanoparticle size is decreased, the bands associated with the classical modes of SnO_2 shift and broaden according to the phonon dispersion curves. Their relationship to nanoparticle size is quite well described by the spatial correlation model, at least for particles larger than 8–10 nm.

With a decrease in grain size two bands appear in the high-frequency region of the spectrum. Our model proposes that these bands are due to a surface layer of nonstoichiometric SnO_2 with different symmetries than SnO_2. The thickness of this layer has been calculated to be ~1.1 nm, i.e., about two to three unit cells, a figure which is consistent with the distorted surface region of any crystalline material.

We believe that the bands which appear in the low-frequency region of the Raman spectrum result from the spherical vibration of the nanoparticles as a whole. Although it is not clear whether these vibrations are due to displacement of atoms at the particle surface, low-frequency Raman scattering proves very effective in providing the complete size distribution of very small nanoparticles. In conclusion, therefore, both the spatial correlation model and low-frequency Raman scattering give a relatively accurate estimation of nanoparticle size in a nondestructive way and the theoretical basis of this has been described.

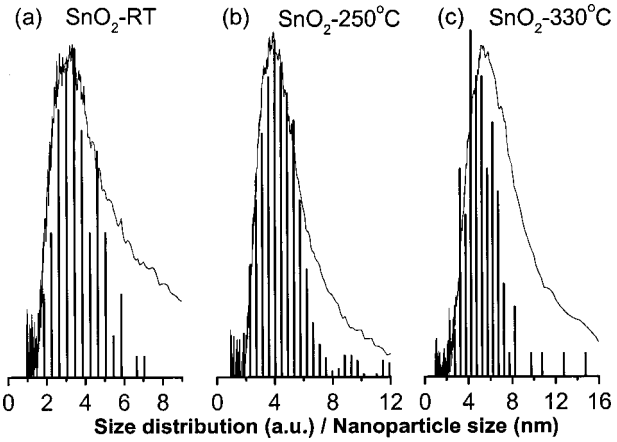

FIG. 8. Comparison of the size distribution obtained by TEM (histograms) and LFR (curves). Note that the values for nanoparticle size differ slightly from those presented in our earlier publication (see Ref. 11). This is due to improved statistics and image processing software.

ACKNOWLEDGMENTS

The author would like to thank Juergen Kappler, Dr. Nicolae Bârsan, and Professor Wolgang Göpel of the Institute of Physical and Theoretical Chemistry of the University of Tübingen for producing the samples. They also thank the European Union (EU) for the financial support given through BRITE-EURAM Contract No. BRE2-CT94-0940 corresponding to project NANOGAS.

[1] Z. M. Jarzebski, J. Electrochem. Soc. **123**, 199C (1976).
[2] R. S. Katiyar, J. Phys. C **3**, 1087 (1970).
[3] J. G. Traylor, H. G. Smith, R. M. Nicklow, and M. K. Wilkinson, Phys. Rev. B **3**, 3457 (1971).
[4] P. Merle, J. Pascual, J. Camassel, and H. Mathieu, Phys. Rev. B **21**, 1617 (1980).
[5] R. S. Katiyar, P. Dawson, M. M. Hargreave, and G. R. Wilkinson, J. Phys. C **4**, 2421 (1971).
[6] R. Summitt, J. Appl. Phys. **39**, 3762 (1968).
[7] P. S. Peercy and B. Morosin, Phys. Rev. B **7**, 2779 (1973).
[8] M. Ocaña, V. Fornés, J. V. García Ramos, and C. J. Serna, J. Solid State Chem. **75**, 364 (1988).
[9] M. Oocaña and C. J. Serna, Spectrochim. Acta, Part A **47**, 765 (1991).
[10] A. Diéguez, A. Romano-Rodríguez, J. R. Morante, U. Weimar, M. Schweizer-Berberich, and W. Göpel, Sens. Actuators B **31**, 1 (1996).
[11] A. Diéguez, A. Romano-Rodríguez, J. R. Morante, N. Bârsan, U. Weimar, and W. Göpel, Appl. Phys. Lett. **71**, 1957 (1997).
[12] J. Zuo, C. Xu, X. Liu, Ch. Wang, Ch. Wang, Y. Hu, and Y. Qian, J. Appl. Phys. **75**, 1835 (1994).
[13] C. Xie, L. Zhang, and Ch. Mo, Phys. Status Solidi A **141**, K59 (1994).
[14] K. N. Yu, Y. Xiong, Y. Liu, and C. Xiong, Phys. Rev. B **55**, 2666 (1997).
[15] L. Abello, B. Bochu, A. Gaskov, S. Koudryavtseva, G. Lucazeau, and M. Roumyantseva, J. Solid State Chem. **135**, 75 (1998).
[16] H. Richter, Z. P. Wang, and L. Ley, Solid State Commun. **39**, 625 (1981).
[17] I. H. Campbell and P. M. Fauchet, Solid State Commun. **58**, 739 (1986).
[18] J. W. Ager III, D. K. Veirs, and G. M. Rosenblatt, Phys. Rev. B **43**, 6491 (1991).
[19] M. Yoshikawa, Y. Mori, H. Obata, M. Maegawa, G. Katagiri, H. Isida, and A. Ishitani, Appl. Phys. Lett. **67**, 694 (1995).
[20] D. Bersani, P. P. Lottici, and X. Z. Ding, Appl. Phys. Lett. **72**, 73 (1998).

[21] T. Werninghaus, J. Hahn, F. Richter, and D. R. T. Zahn, Appl. Phys. Lett. **70**, 958 (1997).
[22] J. Zi, K. Zhang, and X. Xie, Phys. Rev. B **55**, 92 623 (1997).
[23] X. Zhu, R. Birringer, U. Herr, and H. Gleiter, Phys. Rev. B **35**, 9085 (1987).
[24] W. Romanowski, Surf. Sci. **18**, 373 (1969).
[25] F. H. Jones, R. Dixon, J. S. Foord, R. G. Egdell, and J. B. Phetica, Surf. Sci. **376**, 367 (1997).
[26] T. Pagnier, M. Boulova, A. Galerie, A. Gaskov, and G. Lucazeau, J. Solid State Chem. **143**, 86 (1999).
[27] T. Hama and T. Matsubara, Prog. Theor. Phys. **59**, 1407 (1978).
[28] S. Hayashi and K. Yamamoto, Superlattices Microstruct. **2**, 581 (1986).
[29] M. Fujii, T. Nagareda, S. Hayashi, and K. Yamamoto, Phys. Rev. B **44**, 6243 (1991).
[30] L. Saviot, B. Champagnon, E. Duval, I. A. Kudriavtsev, and A. I. Ekimov, J. Non-Cryst. Solids **197**, 238 (1996).
[31] A. Tanaka, S. Onari, and T. Arai, Phys. Rev. B **47**, 1237 (1993).
[32] L. Saviot, B. Champagnon, E. Duval, and A. I. Ekimov, J. Cryst. Growth **184**, 370 (1998).
[33] E. Duval, A. Boukenter, and B. Champagnon, Phys. Rev. Lett. **56**, 2052 (1986).
[34] M. Gotic, M. Ivanda, A. Sekulié, S. Music, S. Popovic, A. Turkovic, and K. Furic, Mater. Lett. **28**, 225 (1996).
[35] H. Lamb, Proc. London Math. Soc. **13**, 189 (1882).
[36] A. Tamura, K. Higeta, and T. Ichinokawa, J. Phys. C **15**, 4975 (1982).